

# Experimental evidence for collisional shock formation via two obliquely merging supersonic plasma jets

Elizabeth C. Merritt,<sup>1,2, a)</sup> Auna L. Moser,<sup>1</sup> Scott C. Hsu,<sup>1, b)</sup> Colin S. Adams,<sup>1,2</sup> and Mark A. Gilmore<sup>2</sup>

<sup>1)</sup> Los Alamos National Laboratory, Los Alamos, NM, 87545, USA

<sup>2)</sup> University of New Mexico, Albuquerque, NM, 87131, USA

(Dated: 19 October 2019)

We report spatially resolved experimental measurements of the oblique merging of two supersonic laboratory plasma jets. The jets are formed and launched by pulsed-power-driven railguns using injected argon, and have electron density  $\sim 10^{14} \text{ cm}^{-3}$ , electron temperature  $\approx 1.4 \text{ eV}$ , ionization fraction near unity, and velocity  $\approx 40 \text{ km/s}$  just prior to merging. The jet merging produces a few-cm-thick stagnation layer, as observed in both fast-framing camera images and multi-chord interferometer data, consistent with collisional shock formation [E. C. Merritt et al., Phys. Rev. Lett. **111**, 085003 (2013)]. The observed stagnation layer emission morphology is consistent with hydrodynamic oblique shock theory at early times, and then undergoes an evolution at later times that is coincident with the theoretically predicted transition to detached shock formation.

## I. INTRODUCTION

We have conducted experiments on the oblique merging of two supersonic plasma jets<sup>1</sup> on the Plasma Liner Experiment<sup>2</sup> (PLX) at Los Alamos National Laboratory (LANL). These experiments were the second in a series of experiments intended to demonstrate the formation of imploding spherical plasma liners via an array of merging supersonic plasma jets.<sup>3–5</sup> The latter has been proposed<sup>3,6,7</sup> as a standoff compression driver for magneto-inertial fusion (MIF)<sup>8–10</sup> and, in the case of targetless implosions, for generating cm-,  $\mu\text{s}$ -, and Mbar-scale plasmas for high energy density (HED) physics<sup>11</sup> research. In our first set of experiments, the parameters and evolution of a single propagating plasma jet were characterized in detail.<sup>2</sup> The next step, a thirty-jet experiment to form and assess spherically imploding plasma liners has been designed<sup>3,5,12</sup> but not yet fielded. A related multi-jet-merging study<sup>13–15</sup> was also conducted recently by our collaborators at HyperV Technologies.

The supersonic jet-merging experiments reported here are also relevant to the basic study of plasma shocks<sup>16</sup> in a semi- to fully collisional regime. Related studies include counter-streaming laser-produced plasmas supporting hohlraum design for indirect-drive inertial confinement fusion<sup>17–19</sup> and for studying astrophysically relevant shocks,<sup>20–24</sup> colliding plasmas using wire-array Z pinches,<sup>25,26</sup> and applications such as pulsed laser deposition<sup>27</sup> and laser-induced breakdown spectroscopy.<sup>28</sup> Primary issues of interest in these studies include the identification of shock formation, the formation of a stagnation layer<sup>29–31</sup> between colliding plasmas, and the possible role of two-fluid and kinetic effects on plasma interpenetration.<sup>32–35</sup>

In this paper we present detailed measurements of the

stagnation layer that forms between two obliquely merging supersonic plasma jets in a semi- to fully collisional regime. First, we briefly describe the experimental setup (Sec. II). Then we discuss observations of the stagnation layer emission morphology (Sec. III) and density enhancements (Sec. IV). We also examine the observed stagnation layer thickness in the context of various estimated collision length scales and two-fluid plasma shock theory (Sec. V). Collectively, our observations are shown to be consistent with oblique collisional shocks and reveal a morphology transition that is coincident with the theoretically predicted transition to detached shocks. We close with a brief discussion of the implications of our results on proposed imploding plasma liner formation experiments (Sec. VI) and a summary (Sec. VII).

## II. EXPERIMENTAL SETUP

Two plasma railguns are mounted on adjacent ports of a 2.7-m-diameter spherical vacuum chamber [Fig. 1(a)], with a half-angle  $\approx 12^\circ$  between the jet axes of propagation and a distance  $\approx 46 \text{ cm}$  between the gun nozzles. Individual jets have peak electron density  $n_e \approx 2 \times 10^{16} \text{ cm}^{-3}$ , peak electron temperature  $T_e \approx 1.4 \text{ eV}$ , diameter = 5 cm, and length  $\approx 20 \text{ cm}$  at the exit of the railgun nozzle.<sup>2</sup> In this series of experiments, the initial jet velocity  $V_{\text{jet}} \approx 40 \text{ km/s}$  and Mach number  $M \equiv V_{\text{jet}}/C_{s,\text{jet}} > 10$ , where  $C_{s,\text{jet}}$  is the sound speed in the jet. More details on the railguns and the characterization of single-jet propagation are reported elsewhere.<sup>2</sup> The jet magnetic field near the railgun bore exit is  $\sim 1 \text{ T}$ , but the classical magnetic diffusion time is a few  $\mu\text{s}$ ,<sup>2</sup> and thus we ignore the effects of a magnetic field by the time of jet merging ( $\approx 20 \mu\text{s}$  later). The jets are individually very highly collisional (thermal mean free paths  $\lambda_i \approx \lambda_e \sim 1 \mu\text{m}$  in a  $\sim 10\text{-cm}$ -scale plasma), but the characteristic interaction length ( $\sim 1 \text{ cm}$ , details given in Sec. V) between counter-propagating jet ions is on the order of the thickness of the observed stagnation layer

<sup>a)</sup> Electronic mail: emerritt@lanl.gov

<sup>b)</sup> Electronic mail: scotthsu@lanl.gov

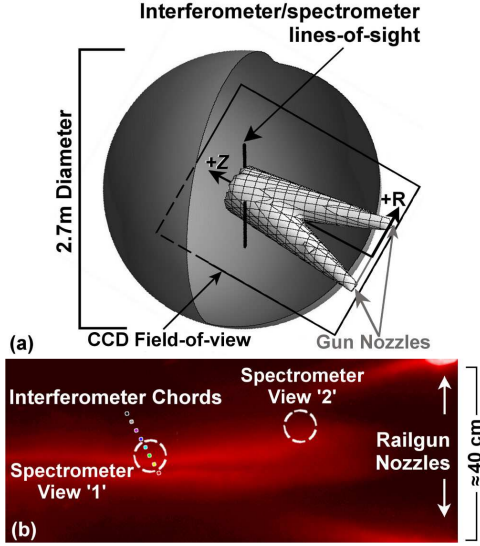


FIG. 1. (a) Schematic showing the spherical vacuum chamber, two merging plasma jets,  $(R, Z)$  coordinates used in the paper, approximate interferometer/spectrometer (spectrometer view '1') lines-of-sight, and CCD camera field-of-view. (b) Location of interferometer chords (dots,  $Z \approx 85$  cm, inter-chord spacing = 1.5 cm), and spectroscopy views (dashed circle, diameter  $\approx 7$  cm) overlaid on a cropped CCD image of jet merging. Spectroscopy views '1' and '2' are located at  $(R, Z) \approx (3.75$  cm, 85 cm) and (12 cm, 55 cm), respectively.

that forms between the obliquely merging jets.

The key diagnostics are a visible-to-near-infrared survey spectrometer (0.275 m focal length with 600 lines/mm grating and  $0.45 \mu\text{s}$  gating on the 1024-pixel microchannel plate array detector), an eight-chord 561 nm laser interferometer,<sup>36,37</sup> and an intensified charged-coupled-device (CCD) visible-imaging camera (DiCam Pro,  $1280 \times 1024$  pixels, 12-bit dynamic range). The CCD camera field-of-view extends from  $Z \approx 0$ –150 cm. The interferometer chords and spectrometer view '1' intersect the stagnation layer at  $Z \approx 85$  cm [Fig. 1(b)]. The interferometer chords are roughly transverse to the stagnation layer, with inter-chord spacing of 1.5 cm, spanning  $R = 0.75$ –11.15 cm. Spectrometer view '1' is centered on the interferometer chord at  $(R, Z) = (3.75$  cm, 85 cm). Spectrometer view '2' is located at  $(R, Z) \approx (12$  cm, 55 cm). The spectrometer field-of-view has a diameter  $\approx 7$  cm. Plasma jet velocity is determined via an array of intensified photodiode detectors.<sup>2</sup> Figure 2 shows a sequence of twelve CCD camera images of the time evolution of jet merging and the formation of a stagnation layer along the jet-merging plane (midplane, horizontal in the images) with a double-peaked emission profile transverse ( $R$  direction, vertical in the images) to the layer. Experiments were conducted with top jet only, bottom jet only, and both jets firing to enable the most direct comparison between single- and merged-jet measurements.

The plasma jet likely had high levels of impurities in these experiments. The post-shot chamber pressure rise for gas injection only was about 30% of that of a full railgun discharge, implying possible plasma impurity levels of 70%. Identification of bright aluminum and oxygen spectral lines in our data<sup>1</sup> suggests that impurities are from the zirconium-toughened-alumina ( $0.15 \text{ ZrO}_2$  and  $0.85 \text{ Al}_2\text{O}_3$ ) railgun insulators. Because the exact impurity fractions as a function of space and time in our jets are unknown, we bound our analysis by considering the two extreme cases of (i) 100% argon and (ii) 30% argon with 70% impurities. For case (ii), we approximate the jet composition as 43% oxygen and 24% aluminum (based on their ratio in zirconium-toughened-alumina) for spectroscopy analysis.

### III. CONSISTENCY OF STAGNATION LAYER MORPHOLOGY WITH HYDRODYNAMIC SHOCKS

During jet merging, an emission structure forms about the jet-interaction plane (Fig. 2), with boundaries that are consistent with collisional oblique shock formation.<sup>1</sup> This is analogous to supersonic flow past a wedge or compression corner.<sup>38,39</sup> We now use analytic one-dimensional (1D) hydrodynamic theory to get a qualitative idea of the shock boundary morphology, and to show that the observed emission layers are consistent with post-shocked plasma, with their edges (at larger  $|R|$ ) corresponding to the shock boundaries.

Figure 3(a) shows a simple schematic of the jet interaction, where  $\delta$  is the angle between the jet flow direction and the midplane,  $M_1$  is the initial (pre-interaction) Mach number, and  $\beta \equiv \beta(\delta, M_1)$  is the angle between the jet-flow direction and the position of an oblique shock boundary.<sup>11,39</sup> Figure 3(b) shows a similar structure in a merged-jet CCD image. In this system, the turning angle  $\delta \equiv \delta(Z_i)$  is given by  $\tan \delta = (23 \text{ cm})/Z_i$ , where  $Z_i$  is the point at which the jets first interact, as determined by the appearance of emission [as indicated in Figs. 3(b) and 3(c)]. Note that the  $Z$  dependence on the horizontal pixel number of the CCD image is nonlinear due to the CCD camera angle. The shock boundary angle  $\beta$  is given by<sup>38</sup>

$$\frac{23 \text{ cm}}{Z_i} = 2 \cot \beta \left[ \frac{M_1^2 \sin^2 \beta - 1}{M_1^2 (\gamma + \cos 2\beta) + 2} \right]. \quad (1)$$

Assuming  $T_e = 1.4$  eV, mean charge  $\bar{Z} = 0.94$  (both inferred from spectroscopy at  $Z = 41$  cm),<sup>2</sup> and specific heat ratio  $\gamma = 1.4$ ,<sup>12</sup> then a 100% argon plasma jet with  $V_{\text{jet}} = 40$  km/s has  $M = 19$ . For the 30%/70% mixture composition,  $T_e = 1.4$  eV and  $\bar{Z} = 0.92$  (Sec. IV), which are similar to the 100% argon case. To place a stringent lower bound on  $M$  for the 30%/70% case, we use an ion-to-proton mass ratio  $\mu = \mu_O = 16$  because oxygen is the lightest element in the impurity mixture. Thus, we estimate that  $12 < M < 19$ . We find that  $\beta - \delta$  values are very similar for  $M = 12$  and  $M = 19$  for a range of

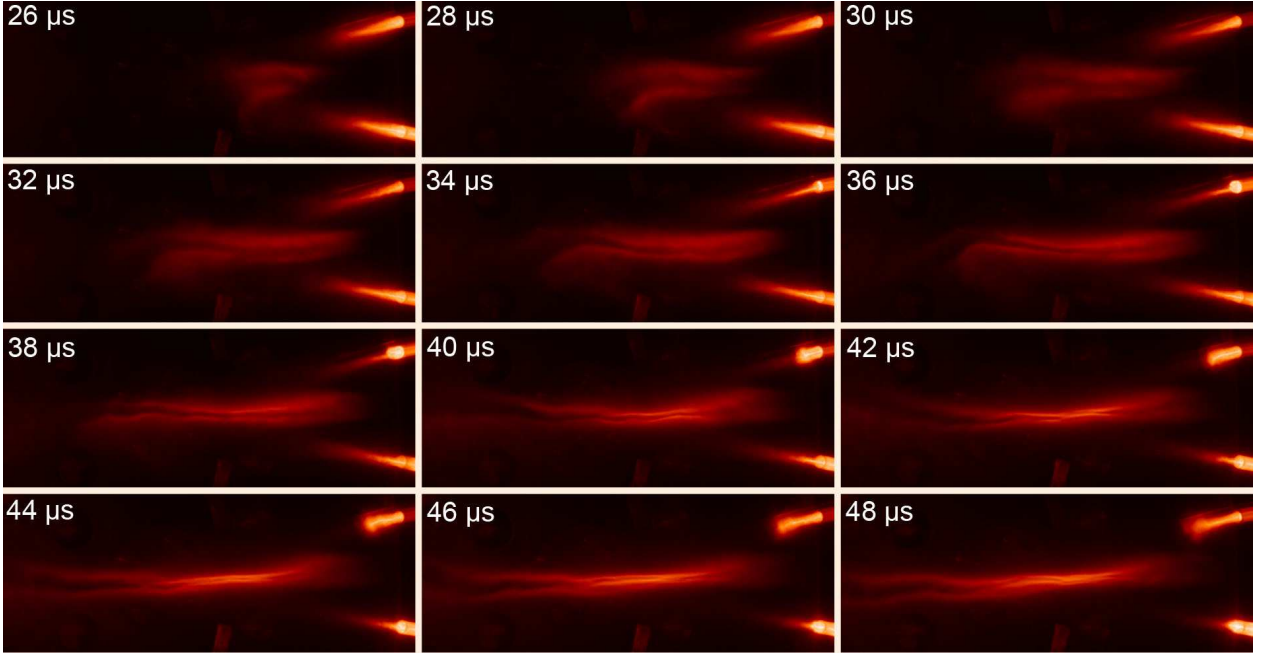


FIG. 2. False-color, cropped CCD images (log intensity, 20 ns exposure) of oblique jet merging [shots 1130, 1129, 1128, 1127, 1125, 1122, 1120, 1132, 1134, 1136, 1138, 1140 (in order of timing)]. In each image, the two railgun nozzles ( $\approx 46$  cm apart) are visible on the right-hand-side and the stagnation layer is oriented horizontally.

$Z$  [Fig. 4(a)]. We observe that  $Z_i$  falls from  $Z_i \approx 45$  cm at  $t = 26 \mu\text{s}$  to  $Z_i \approx 18$  cm at  $t = 36 \mu\text{s}$  [Fig. 4(b)]. A second peak in  $Z_i$  at  $t \approx 45 \mu\text{s}$  is due to a trailing jet (created by ringing in the underdamped railgun current<sup>2</sup>) reaching the merge region.

One-dimensional oblique shock theory predicts a maximum turning angle  $\delta_{\text{max}}$  (for a given  $M$ ) for which an oblique shock will form. For  $M = 12$ –19,  $\delta_{\text{max}} \approx 45^\circ$ , corresponding to  $Z_i \approx 25$  cm [vertical dotted line in Fig. 4(a)]. Thus for  $Z_i \gtrsim 25$  cm, we expect the merged-jet envelope to resemble the wedge-shaped structures shown in Figs. 3(a) and 3(b). For  $t \approx 24$ –33  $\mu\text{s}$  [see Fig. 4(b)],  $Z_i$  values predict oblique shock formation consistent with the observed wedge-shaped emission boundary, as marked in Fig. 3(b), where  $Z_i \approx 30$  cm. In this case, the measured  $\beta - \delta \approx 5^\circ$ . For  $M = 12$ –19, the theoretically predicted  $\beta - \delta \approx 11^\circ$ , which is within approximately a factor of two of the experimentally inferred value. This is reasonable agreement given that the 1D prediction does not include 3D nor plasma equation-of-state<sup>14</sup> effects. For  $\delta > \delta_{\text{max}}$  ( $Z_i < 25$  cm), 1D theory predicts detached rather than oblique shocks. In the experiment, we find that the emission boundary morphology changes from a wedge shape to a thinner emission layer concentrated along the midplane [Fig. 3(c)]. This transition, corresponding to the theoretical threshold at  $\delta_{\text{max}}$ , is approximately coincident with the observation of  $Z_i$  falling below  $\approx 25$  cm at  $t \approx 33 \mu\text{s}$ .

#### IV. OBSERVATION OF MERGED-JET DENSITIES EXCEEDING THAT OF INTERPENETRATION

If the merged-jet emission layers are post-shocked plasma, then we expect an increase in density across the shock boundary during jet merging. The density increase across a 1D shock boundary should satisfy the 1D Rankine-Hugoniot relation<sup>11</sup>

$$\frac{n_2}{n_1} = \frac{(M_1 \sin \beta)^2 (\gamma + 1)}{(M_1 \sin \beta)^2 (\gamma - 1) + 2}, \quad (2)$$

where  $n_1$  and  $n_2$  are the pre- and post-shock densities, respectively. We bound the theoretically predicted density changes in the system by using the range  $M_1 = 12$ –19, as well as the  $\beta$  range corresponding to the observed  $Z_i(\delta)$ . Because the  $Z_i$  range encompasses  $\delta > \delta_{\text{max}}$ , we must consider the limiting case of detached shock formation (corresponding to a normal shock, i.e.,  $\beta = 90^\circ$ , in 1D theory) in addition to oblique shocks. For an oblique shock with  $M = 12$ , Eq. (1) gives  $\beta = 34^\circ$ – $59^\circ$  for measured  $Z_i = 45$ –25 cm. Thus, the range of  $n_2/n_1 = 5.4$ –5.7. Similarly, for  $M = 19$  we find  $\beta = 34^\circ$ – $58^\circ$  and  $n_2/n_1 = 5.7$ –5.9. Assuming normal shocks ( $\beta = 90^\circ$ ) for  $Z_i < 25$  cm, we find  $n_2/n_1 = 5.8$ –5.9 for  $M = 12$ –19. Thus, the overall range across the shock boundary is  $n_2/n_1 = 5.4$ –5.9, according to 1D theory.

Next we compare  $n_2/n_1$  from the 1D theory with the measured density enhancement  $n_{\text{merged}}/n_{\text{single}}$  of the merged- over single-jet cases. We calculate the ion-plus-neutral density  $n_{\text{tot}}$  using an interferometer phase shift

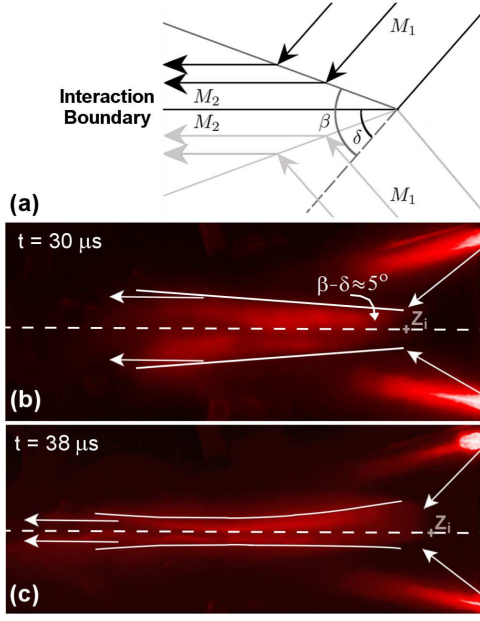


FIG. 3. (a) Simple schematic of the interaction of two obliquely interacting supersonic flows with initial Mach numbers  $M_1$ . Flows are incident on the midplane with angle  $\delta$ . A shock boundary forms at angle  $\beta$  with respect to the original flow direction. Post-shock flows have Mach number  $M_2$  and flow direction parallel to the midplane. (b) CCD image with postulated shock boundaries (solid white lines) and initial jet interaction distances  $Z_i$  for shot 1128 at  $t = 30 \mu\text{s}$  and (c) shot 1120 at  $t = 38 \mu\text{s}$ .

analysis accounting for multiple ionization states and the presence of impurities (see Appendix). According to Eq. (A6), to determine  $n_{\text{tot}}$  we need the interferometer phase shift  $\Delta\phi$ , mean charge  $\bar{Z}$ , the correction  $Err$  [Eq. (A5)] accounting for all non-free-electron contributions to  $\Delta\phi$ , and the interferometer chord path length (approximated by the plasma jet diameter). The maximum correction  $Err_{\text{max}}$  is the largest scaled sensitivity,  $C_{0,k}/C_e$  [Eq. (A9)]. These are for Ar I:  $0.08$  ( $\delta N_n^{STP} = 2.8 \times 10^{-4}$  at  $\lambda = 561 \text{ nm}$ ,  $\rho^{STP} = 1.6 \text{ g/L}$ ),<sup>40,41</sup> for O I:  $0.03$  ( $K_{OImO} \approx 4.4 \times 10^{-36} \text{ cm}^3$  for  $5000 \text{ K} < T < 10000 \text{ K}$ ),<sup>42</sup> and for Al I:  $0.007$  ( $\delta N_n^{STP} = 6.2 \times 10^{-2}$  at  $\lambda = 561 \text{ nm}$ ,  $\rho^{STP} = 2.7 \text{ g/cm}^3$ ).<sup>41,43</sup> Thus,  $Err_{\text{max}} = 0.08$  (for Ar I).

First, we determine  $\Delta\phi_{\text{single}}$  and  $\Delta\phi_{\text{merged}}$  for the single- and merged-jet cases, respectively. The single-jet peak  $\Delta\phi_{\text{single}}$ , averaged across chords for a single shot, is  $\Delta\phi_{\text{single}} \approx 4.0^\circ \pm 0.6^\circ$ , where  $0.6^\circ$  is the standard deviation [Fig. 5(a)]. The peak  $\Delta\phi_{\text{single}}$  averaged over multiple top-jet-only shots at the  $R = 2.25 \text{ cm}$  chord is  $\Delta\phi_{\text{single}} = 4.3^\circ \pm 0.3^\circ$  [Fig. 6(b)], and thus we assume  $\Delta\phi_{\text{single}} = 4.0^\circ$  for evaluating  $n_{\text{tot,single}} \equiv n_{\text{single}}$ . Merged-jet  $\Delta\phi_{\text{merged}}$  traces for a single shot show [Fig. 5(b)] a non-uniform spatial profile with a peak near the midplane and peak magnitude  $\Delta\phi \approx 14^\circ$ . At  $R = 2.25 \text{ cm}$ , the peak  $\Delta\phi = 14.3 \pm 2.4^\circ$  aver-

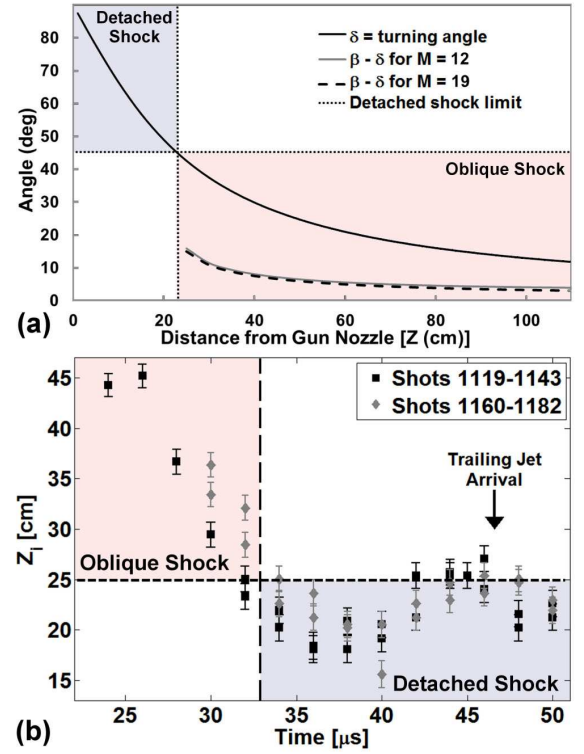


FIG. 4. (a) Plot of  $\delta$  and  $\beta - \delta$  vs.  $Z$  for both  $M = 12$  and  $M = 19$  (from 1D hydrodynamic theory). The predicted threshold turning angle,  $\delta = \delta_{\text{max}} = 45^\circ$ , and corresponding  $Z_i(\delta_{\text{max}}) \approx 25 \text{ cm}$  are marked with horizontal and vertical dotted lines, respectively. (b) Plot of  $Z_i$  vs. time for shots 1119–1143 and shots 1160–1182. Error bars correspond to a  $\pm 7.5$  pixel offset along the  $Z$  axis during image processing. The theoretical cutoff for oblique shock formation,  $Z_i \approx 25 \text{ cm}$ , is marked by a horizontal dashed line.

aged over multiple shots [Fig. 6(b)]. Thus, we assume  $\Delta\phi_{\text{merged}} = 14.0^\circ$  for evaluating  $n_{\text{tot,merged}} \equiv n_{\text{merged}}$ .

Before evaluating  $n_{\text{single}}$  and  $n_{\text{merged}}$ , we examine  $\Delta\phi$  enhancements for merged- over single-jet experiments by considering the quantity

$$\Delta\psi = \Delta\phi_{\text{merged}} - (\Delta\phi_{\text{top}} + \Delta\phi_{\text{bottom}}), \quad (3)$$

where  $\Delta\phi_{\text{top}}$  and  $\Delta\phi_{\text{bottom}}$  are from top-jet-only and bottom-jet-only shots, respectively. A  $\Delta\psi > 0$  implies a density of the merged-jet beyond that of the sum of single jets and/or an increase in  $\bar{Z}$  over that of a single jet. Merged-jet measurements over the data set considered (merged-jet: shots 1117–1196; bottom-jet: shots 1277–1278; top-jet: shots 1265–1267) show that  $\Delta\psi > 0$  for  $R \leq 5.25 \text{ cm}$  [Fig. 6(a)], implying that simple jet interpenetration cannot account for the observed stagnation layer  $\Delta\phi_{\text{merged}}$ . For  $R \geq 6.75 \text{ cm}$ ,  $\Delta\psi$  is small because this region is beyond the stagnation layer.

Now we evaluate  $n_{\text{single}}$  and  $n_{\text{merged}}$  in order to estimate the density enhancement  $n_{\text{single}}/n_{\text{merged}}$  at  $Z \approx 85 \text{ cm}$  and  $R \leq 5.25 \text{ cm}$ . A single jet (assuming 100% Ar)



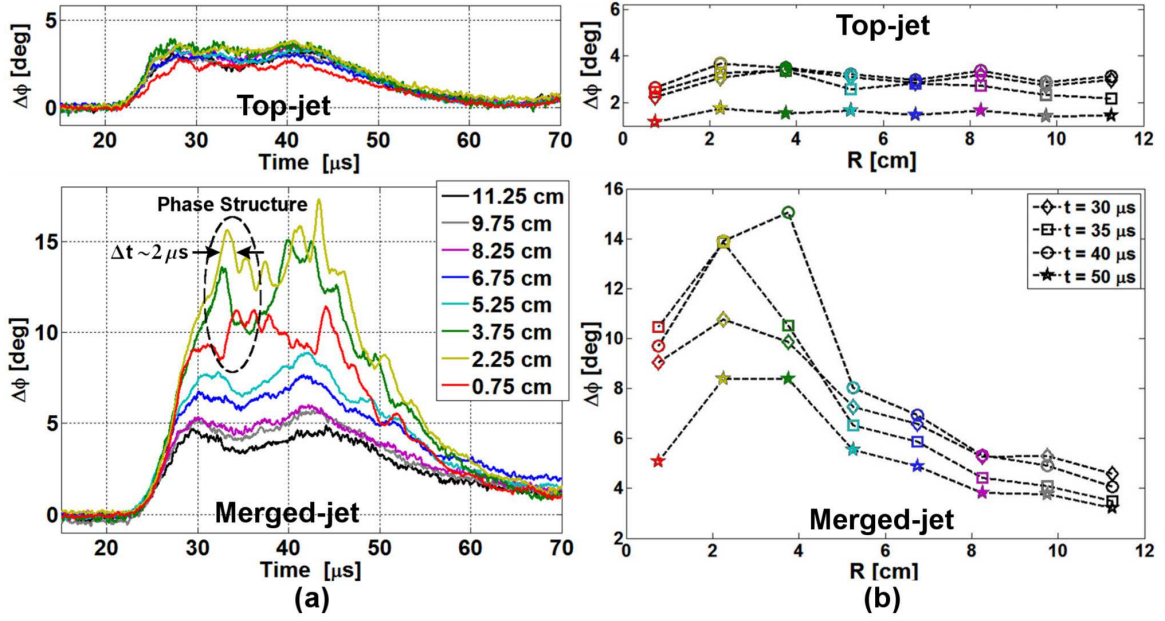


FIG. 5. (a) Phase shift vs. time at  $Z \approx 85$  cm for top-jet-only (shot 1265) and merged-jet (shot 1120) cases. The merged-jet phase shift shows multiple small phase peaks of amplitude  $\approx 2.5^\circ$  and width  $\Delta t \approx 2 \mu$ s. One such phase structure is highlighted by the dashed circle. (b) Phase shift vs. interferometer chord position at several times for the same shots.

has  $\bar{Z} = 0.94$  at  $Z \approx 41$  cm and a jet diameter  $\approx 22$  cm at  $Z \approx 80$  cm.<sup>2</sup> Using these values with  $\Delta\phi_{\text{single}} = 4.0^\circ$ , we obtain  $n_{\text{single}} = 2.1\text{--}2.3 \times 10^{14} \text{ cm}^{-3}$  (bounds provided by  $Err = 0$  and  $Err_{\text{max}} = 0.08$ ). The  $\bar{Z}$ , and therefore the  $n_{\text{single}}$  estimate, changes by only a few percent for the 30%/70% mixture.<sup>1</sup>

For the merged-jet case, we infer  $\bar{Z}$  and  $T_e$  at  $Z \approx 85$  cm by comparing merged-jet spectroscopy data<sup>1</sup> (from view ‘1’) with non-local-thermodynamic-equilibrium (non-LTE) spectral calculations using PrismSPECT.<sup>44</sup> The PrismSPECT calculations for  $\bar{Z}$  and  $T_e$  are sensitive to the specific plasma mixture used. Based on the presence of certain Ar II lines in the data and by comparing to PrismSPECT results, we bound estimates of  $\bar{Z}$  and  $T_e$  using the 100% argon and 30%/70% mixture cases. For the former, we infer that peak  $T_e \geq 1.4$  eV and  $\bar{Z} \geq 0.94$ .<sup>1</sup> For the latter, we infer that  $2.2 \text{ eV} \leq \text{peak } T_e < 2.3 \text{ eV}$  and  $1.3 \leq \bar{Z} < 1.4$ , with the upper bounds determined by the absence of an Al III line in the data.<sup>1</sup> Thus, for the 100% argon case, we see little change in  $\bar{Z}$  compared to the single-jet measurements, but the 30%/70% mixture calculation predicts an increase in  $\bar{Z}$  during jet merging, accounting for some of the observed  $\Delta\phi$  enhancement. Using  $\Delta\phi = 14^\circ$ , chord path length of 22 cm, and  $\bar{Z} = 0.94$  (100% argon case), we obtain  $n_{\text{merged}} = 7.5\text{--}8.2 \times 10^{14} \text{ cm}^{-3}$  (bounds provided by  $Err = 0$  and  $Err_{\text{max}} = 0.08$ ). In this case the density increase  $n_{\text{merged}}/n_{\text{single}} = 3.2\text{--}3.8$ . For the most conservative  $\bar{Z} = 1.4$  (30%/70% mixture case),  $n_{\text{merged}} = 5.0\text{--}5.3 \times 10^{14} \text{ cm}^{-3}$ , and  $n_{\text{merged}}/n_{\text{single}} = 2.1\text{--}2.4$ . These values are summarized in Table I. The smaller density

increase for the 30%/70% mixture case is consistent with an increased  $\bar{Z}$  in that case.

The observed range of  $n_{\text{merged}}/n_{\text{single}} = 2.1\text{--}3.8$  exceeds the factor of two expected for jet interpenetration, although it is smaller than the  $n_2/n_1 = n_{\text{shock}}/n_{\text{unshocked}} = 5.4\text{--}5.9$  predicted by 1D theory. Note that plasma diameter enhancement (along the interferometer chord direction) in the merged- over the single-jet case, which we have not characterized, and overestimates of  $\bar{Z}$  (given that we do not have a direct measurement at  $Z \approx 85$  cm) would both lead to reductions in our estimate of  $n_{\text{merged}}/n_{\text{single}}$ . The difference between the measured and predicted density jumps could be due to 3D (e.g., pressure-relief in the out-of-page dimension) and/or plasma equation-of-state effects not modeled by 1D hydrodynamic theory.

We point out a few additional features from the interferometry. The spatial profile for the merged-jet  $\Delta\phi$ , as seen in Fig. 5(b), is peaked a few centimeters away from the midplane ( $R = 0$ ) and correlates with the peaked emission profile in the  $R$  direction, as seen in the CCD images (Fig. 2). Figure 5(a) shows evidence of variations in  $\Delta\phi_{\text{peak}} \approx 2.5^\circ$  over  $\Delta t \approx 2 \mu$ s in the merged-jet measurements that are not present in single-jet experiments. Assuming  $V_{\text{jet}} = 40 \text{ km/s}$ , the width of the indicated structure is  $\approx 8$  cm. The appearance of this  $\Delta\phi$  structure alternates between adjacent chords for chords at  $R = 0.75\text{--}3.75$  cm, i.e., the  $\Delta\phi$  rise in one chord corresponds to a fall in another chord at  $\approx 1.5 \mu$ s intervals. Because the inter-chord distance is 1.5 cm, the structure has a transverse velocity  $\approx 15 \text{ km/s}$ . The underlying

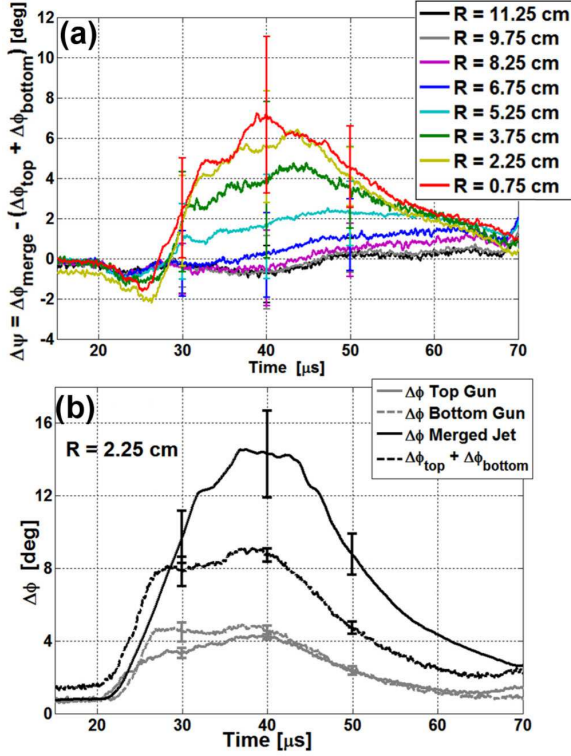


FIG. 6. (a) The difference between merged-jet and the sum of single-jet phase shifts  $\Delta\psi$  vs. time for data averaged over shots 1117–1196 (merged-jet), shots 1277–1278 (bottom-jet) and shots 1265–1267 (top-jet). (b) Multi-shot (same data sets) averaged interferometer phase shift vs. time at  $R = 2.25$  cm, for top-, bottom-, and merged-jet cases. Error bars indicate the standard deviation of  $\Delta\psi$  or  $\Delta\phi$  over the stated data set.

cause of these structures has not yet been determined.

Electron density results (determined via Stark broadening of the H- $\beta$  line) at spectrometer view ‘2’ ( $Z \approx 55$  cm) also show a density enhancement: from  $n_e \leq 8.6 \times 10^{13} \text{ cm}^{-3}$  (shot 1106) for a top-jet-only case to  $n_e \approx 1.6 \times 10^{15} \text{ cm}^{-3}$  (shot 1101) during jet merging

	100% Ar	30%/70%
$T_{e,\text{merged}}$	$\geq 1.4 \text{ eV}$	$2.2 \text{ eV} \leq T_e < 2.3 \text{ eV}$
$\bar{Z}_{\text{single}}$	0.94	0.92
$\bar{Z}_{\text{merged}}$	0.94	1.4
$n_{\text{single}}$	$2.1\text{--}2.3 \times 10^{14} \text{ cm}^{-3}$	$2.2\text{--}2.4 \times 10^{14} \text{ cm}^{-3}$
$n_{\text{merged}}$	$7.5\text{--}8.2 \times 10^{14} \text{ cm}^{-3}$	$5.0\text{--}5.3 \times 10^{14} \text{ cm}^{-3}$
$n_{\text{single}}/n_{\text{merged}}$	3.2–3.8	2.1–2.4

TABLE I. Summary of the experimentally inferred jet density enhancement at  $Z \approx 85$  cm for the two mixture cases: 100% Ar and 30% Ar/70% impurities. Single-jet and merged-jet densities are calculated using  $\Delta\phi = 4^\circ$  and  $\Delta\phi = 14^\circ$ , respectively, jet diameter of 22 cm, and  $\text{Err}_{\text{max}} = 0.08$ . Note that values for  $\bar{Z}_{\text{single}}$  are from  $Z \approx 41$  cm.<sup>2</sup>

(Fig. 7). The electron density was determined via<sup>2</sup>

$$n_e = 6.05 \times 10^{14} [\text{FWHM}(\text{pixels})]^{3/2} \text{ cm}^{-3}, \quad (4)$$

where FWHM is the full-width-half-maximum of the Stark-broadened H- $\beta$  line (more details given in the caption for Fig. 7). For the top-jet-only shot (1106), the FWHM of the Lorentzian (with instrumental broadening removed) is 0.27 pixels, which is significantly less than the 1 pixel spectrometer resolution. So, we consider  $n_e = 8.6 \times 10^{13} \text{ cm}^{-3}$  an upper bound, i.e., the density could be less but is too small to be resolvable. Thus,  $n_{e,\text{merged}}/n_{e,\text{single}} \gtrsim 10$  at  $Z \approx 55$  cm, which is significantly larger than the  $n_{\text{merged}}/n_{\text{single}}$  observed at  $Z \approx 85$  cm. Some of the  $n_e$  increase is likely due to increased ionization during jet merging, but unfortunately there was not enough information in the measured spectrum at  $Z \approx 55$  cm to infer  $\bar{Z}$ . The magnitude of the  $n_e$  enhancement suggests the presence of post-shocked density also at  $Z \approx 55$  cm.

## V. COLLISIONALITY ESTIMATES AND COMPARISON TO TWO-FLUID PLASMA SHOCK THEORY

Both the experimentally measured emission<sup>1</sup> and interferometer  $\Delta\phi$  [Fig. 5(b)] have the same gradient length scale (few cm) in the  $R$  direction, and the  $\Delta\phi$  dip at  $R = 0.75$  cm and peak at  $R = 2.24\text{--}3.75$  cm [Fig. 5(b)] are well-aligned with the emission dip and peak, respectively.<sup>1</sup> In this section, we compare these observations with the expected scale size of a collisional plasma shock. In the case of colliding plasmas, the shock scale length is expected<sup>34</sup> to be on the order of the ion penetration length into the opposing jet. After evaluating both transverse diffusion and slowing down frequencies,<sup>45</sup> we find that, in our parameter regime, the limiting physics for ion penetration is frictional drag exerted by the ions of one jet on the counter-streaming ions of the other jet. This is evaluated using the slowing-down rate  $\nu_{ii'}^s$  in the fast approximation,<sup>45</sup>

$$\nu_{ii'}^s = 9.0 \times 10^{-8} n_i' Z'^2 \ln \Lambda \left( \frac{1}{\mu} + \frac{1}{\mu'} \right) \frac{\mu^{1/2}}{\epsilon^{3/2}}, \quad (5)$$

where the unprimed and primed variables correspond to a test particle from one jet and the field particles of the other jet, respectively. The ion penetration length is

$$\lambda_{ii'}^s \approx v_{\text{rel}} / 4\nu_{ii'}^s, \quad (6)$$

where  $v_{\text{rel}}$  is the relative transverse velocity between obliquely merging jets, and the factor of 4 results from the integral effect of  $v_{\text{rel}}$  slowing down to zero.<sup>14</sup> We estimate  $\lambda_{ii'}^s$  by considering jets of 100% argon and the 30%/70% mixture (specifically, 30% Ar, 43% O, 24% Al), in all cases using  $v_{\text{rel}} = 20 \text{ km/s}$  and the plasma parameters listed in Table II, which also contains a summary of the various length estimates (ion-electron slowing-down

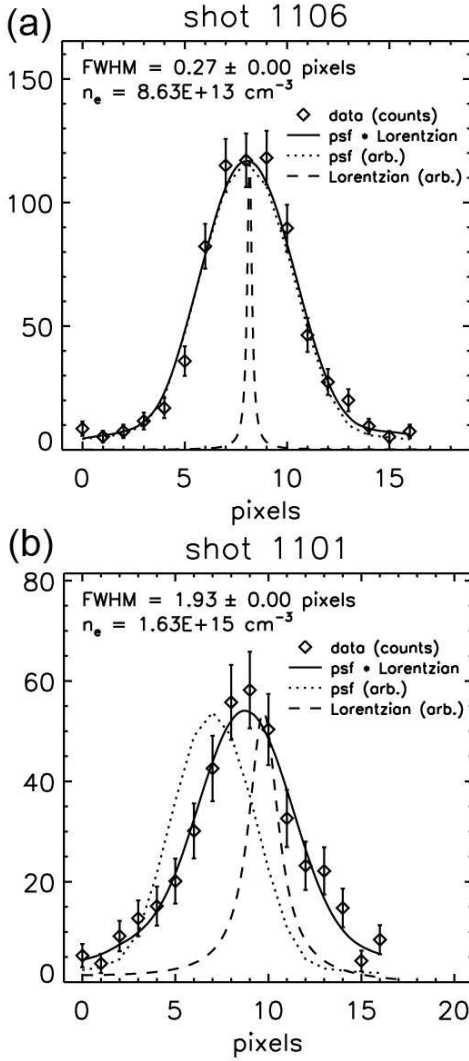


FIG. 7. Determination of electron density  $n_e$  at  $t = 30 \mu\text{s}$  via Stark broadening of the H- $\beta$  lines for (a) top-jet-only (shot 1106) and (b) merged-jet (shot 1101) cases at the spectrometer position ‘2’ [see Fig. 1(b)]. Shown are the experimental data (diamonds with error bars  $\pm\sqrt{\text{counts}}$ ), an overlay of the measured instrumental broadening profile (dotted line, labeled as ‘psf’ for point spread function), and a Lorentzian H- $\beta$  profile (dashed line) that gives the best fit (minimum  $\chi^2$ ) of the convolution (solid line) of the psf and the Lorentzian to the data.

distance  $\lambda_{ie}^s$ , using the slow approximation for  $\nu_{ie}^s$ , is also included for comparison). For inter-species collisions in a mixed-species jet (due to impurities), we use  $n_i = (\% \text{ ion species}) \times n_{\text{tot}}$ .

We also estimate the inter-jet mean free path (mfp) of  $\text{Ar}^{1+}$ -Ar charge and momentum transfer. The assumption of  $v_{\text{rel}} = 20 \text{ km/s}$  gives a kinetic energy of  $\approx 80 \text{ eV}$ , corresponding to charge and momentum transfer cross-sections  $\sigma_{CT} \approx 0.3 \times 10^{-18} \text{ m}^2$  and  $\sigma_m \approx 0.7 \times 10^{-18} \text{ m}^2$ , respectively.<sup>46</sup> The total mfp for  $\text{Ar}^{1+}$ -Ar interaction is  $\lambda_{in} = 1/\sigma_{\text{tot}}n_n = 1/[(\sigma_{CT} + \sigma_m)n_n]$ , where  $n_n =$

	100% Ar	30%/70%
$n_{\text{tot}}$	$8 \times 10^{14} \text{ cm}^{-3}$	$5 \times 10^{14} \text{ cm}^{-3}$
$T_e$	1.4 eV	2.2 eV
$\bar{Z}$ Ar	0.94	1.2
Al		2.0
O		1.0
$\lambda_{ii'}^s$ Ar-Ar	3.47 cm	2.03 cm
Al-Al		0.16 cm
O-O		0.62 cm
Interspecies		0.57–6.18 cm
$\lambda_{ie}^s$ Ar	19.4 cm	25.6 cm
Al		6.73 cm
O		14.4 cm

TABLE II. Summary of stopping lengths for inter-jet particle interactions, for both the 100% Ar and 30%/70% mixture cases.

$(1 - \bar{Z})n_{\text{tot}}$  (for  $\bar{Z} < 1$ ) is the neutral density. For 100% argon merged-jet parameters,  $\lambda_{in} \approx 2 \text{ cm} \sim \lambda_{ii'}^s$ . Comparing all these length scale estimates with the observed few-cm-thick stagnation layer implies that our inter-jet merging is in a semi- to fully collisional regime.

Previously, we showed that the transverse ( $R$ ) dynamics of our oblique jet merging compared favorably with 1D collisional multi-fluid plasma simulations of our experiment.<sup>1</sup> Here, we consider our experimental observations in the context of two-fluid plasma shock theory.<sup>16</sup> In the case of a high- $M$ , two-fluid shock, differing ion and electron transport results in shock structures on multiple spatial scales.<sup>16</sup> The length scale of ion viscosity and thermal conduction effects is on the order of the collisional mfp of the shocked ions,  $\lambda_i = v_{ti}/\nu_i$ , where  $v_{ti}$  and  $\nu_i$  are the ion thermal velocity and thermal collision frequency, respectively, while the length scale of electron viscosity and thermal conduction effects is on the order of  $\lambda_i \sqrt{m_i/m_e}$ .<sup>16</sup> The range of downstream mfp in our system is estimated to be between  $6.4 \times 10^{-3} \text{ cm}$  (minimum, from the 30%/70% mixture) and  $3.2 \times 10^{-2} \text{ cm}$  (maximum, from pure argon) based on the merged-jet parameters given in Table I. In order to bound the range of electron shock scale lengths, we use the limiting cases of  $\mu = \mu_O = 16$  and  $\mu = \mu_{Ar} = 40$ , and obtain  $\lambda_i \sqrt{m_i/m_e} \approx 1.1\text{--}8.6 \text{ cm}$ , which is of the same order as the gradient scale length of the observed emission<sup>1</sup> and  $\Delta\phi$  profiles [Fig. 5(b)]. This implies that our observations are consistent with a collisional two-fluid plasma shock.

## VI. ON THE USE OF MERGING PLASMA JETS FOR FORMING SPHERICALLY IMPLoding PLASMA LINERS

A key motivation for this work was to study two obliquely merging supersonic plasma jets as the ‘unit physics’ process underlying the use of an array of such

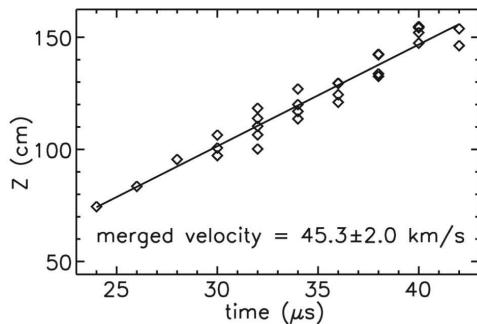


FIG. 8. Leading edge position of the merged jet, as determined visually from CCD images, versus time (shots 1120–1172). Diamonds are data points, and the black line is a linear fit giving the velocity of the merged-jet leading edge.

jets to form spherically imploding plasma liners. The latter is envisioned as a standoff driver for MIF.<sup>2,3,6,7,47,48</sup> The dynamics arising in the jet merging, e.g., shock formation, sets the properties of the subsequent, merged plasma that ultimately determines the liner uniformity and peak ram pressure ( $\rho v^2$ ). These physics issues have been considered recently via theory and numerical modeling.<sup>4,49,50</sup> In spherical plasma liner formation via an array of plasma jets, the initial merging would be among more than two jets, and the detailed merging geometry would depend on the port geometry of the vacuum chamber. In the case of PLX, a quasi-spherical arrangement of 60 plasma guns would result in twelve groups of five jets, with each group arranged in a pentagonal pattern.

A key figure of merit for implosion performance is the jet/liner Mach number  $M$ , i.e., a lower  $M$  results in faster plasma spreading, density reduction, and lower ram pressure.<sup>5,12,49,51</sup> The *a priori* concern was that jet merging would lead to shock formation and heating that would significantly decrease  $M$  (compared to its initial value) and, thus, implosion performance. The results reported here are encouraging in that the experimentally inferred increases in  $T_e$  [by up to a factor of  $(2.3 \text{ eV})/(1.4 \text{ eV}) = 1.64$ ] and  $\bar{Z}$  (by up to a factor of  $1.4/0.94 = 1.49$ ) lead to an increase in  $C_s \sim (\bar{Z}T_e)^{1/2}$  of 56%. We estimate the speed of the leading edge of the merged plasma to be  $\approx 45 \text{ km/s}$  (see Fig. 8), which is close to the initial jet speed of  $\approx 41 \text{ km/s}$ . An unchanged velocity after jet merging would result in a modest 36% reduction in  $M$ .

With regard to uniformity, the outstanding questions are how the observed structure in two-jet merging would affect the uniformity of the leading edge of an imploding spherical plasma liner formed by multiple merging jets, and how much non-uniformity would be tolerable for compression of a magnetized plasma target for application to MIF. This problem has been studied recently in two simulation studies,<sup>4,50</sup> which reached opposing conclusions using two different codes employing very different numerical models and techniques. One

study concluded that a series of shocks occurring during plasma liner convergence would degrade the implosion performance,<sup>50</sup> while the other showed that initial non-uniformities arising from jet merging were largely smeared out by the time of peak compression.<sup>4</sup> More detailed studies are needed to resolve the discrepancy. We envision a five-jet experiment on PLX followed by a 30- or 60-jet experiment to study this and other issues.

## VII. SUMMARY

In summary, we have made spatially resolved measurements, in a semi- to fully collisional regime, of the stagnation layer that forms between two obliquely merging supersonic plasma jets. CCD images show a double-peaked emission profile transverse to the layer, with the central emission dip consistent with a density dip observed in the interferometer data. The stagnation layer thickness is a few cm, which is of the same order as the ion penetration length (in our case determined by frictional drag between counter-streaming ions). The observed stagnation layer emission morphology is consistent with hydrodynamic oblique shock theory at early times, and undergoes an evolution at later times that is coincident with the theoretically predicted transition to detached shock formation. The density increase from that of an individual jet to the density of the post-merge stagnation layer is greater than that of interpenetration, even accounting for the higher ionization estimates found for the high impurity versus pure argon analysis limits. The measured density increase is low compared to 1D theoretical hydrodynamic predictions, but discrepancies are expected due to multi-dimensional and plasma equation-of-state effects in the experiment. We did not observe a strong rise in  $T_e$  or  $\bar{Z}$ , which, coupled with little observed change in the jet velocity after merging, is encouraging for proposed plasma liner formation experiments.

## ACKNOWLEDGMENTS

Significant portions of this work are from E. C. Merritt's doctoral dissertation. We acknowledge J. P. Dunn (LANL) for experimental support, HyperV Technologies Corp. for extensive advice on railgun operation, and J. T. Cassibry (University of Alabama, Huntsville) for useful discussions. This work was supported by the U.S. Department of Energy.

## Appendix A: Interferometer phase shift analysis

Previous interferometer phase shift analysis<sup>37</sup> for this experiment assumed a singly ionized argon plasma, which was adequate for our single-jet experiments.<sup>2</sup> In these two-jet merging experiments, the observation of higher



ionization states and significant impurity percentages required generalization of the phase shift analysis.

For a plasma with multiple gas species and ionization states, we can write  $\Delta\phi$  as a superposition of the contributions from the electrons and all possible ionization states for each gas species in the plasma:

$$\Delta\phi_{\text{tot}} = \Delta\phi_e - \sum_{j,k} \Delta\phi_{j,k} \quad (\text{A1})$$

$$= \int C_e n_e dl - \int \sum_{j,k} C_{j,k} n_{j,k} dl, \quad (\text{A2})$$

where  $j$  is the atom ionization state,  $j = 0$  denotes a neutral atom,  $k$  is the gas species, and  $C_{j,k}$  is the interferometer sensitivity constant for a given gas species and ionization state.

For a species with ionization state  $j$ , the electron density due to that species is  $n_{e,j} = j n_j$ . The total electron density is then  $n_e = \sum_{j,k} n_{e,(j,k)} = \sum_{j,k} j n_{j,k}$ . The average ionization state of the plasma is then

$$\bar{Z} = \frac{n_e}{n_{\text{tot}}} = \frac{\sum_{j,k} n_{e,(j,k)}}{\sum_{j,k} n_{j,k}} = \frac{\sum_{j,k} j n_{j,k}}{\sum_{j,k} n_{j,k}}, \quad (\text{A3})$$

where  $n_{\text{tot}} = \sum_{j,k} n_{j,k}$  is the total atomic density of the plasma. The phase shift equation becomes

$$\begin{aligned} \Delta\phi_{\text{tot}} &= \int \left[ C_e \bar{Z} n_{\text{tot}} - \sum_{j,k} C_{j,k} n_{j,k} \right] dl \\ &= \int C_e \left[ \bar{Z} - \sum_{j,k} \frac{C_{j,k}}{C_e} \frac{n_{j,k}}{n_{\text{tot}}} \right] n_{\text{tot}} dl \\ &\approx C_e [\bar{Z} - \text{Err}] \int n_{\text{tot}} dl, \end{aligned} \quad (\text{A4})$$

assuming a uniform average charge state along the path length through the plasma, and where

$$\text{Err} = \sum_{j,k} \frac{C_{j,k}}{C_e} \frac{n_{j,k}}{n_{\text{tot}}}. \quad (\text{A5})$$

If all the sensitivity constants for all species and ionization states in the plasma are known, then the error can be calculated exactly. However, many indices of refraction for ionized materials, and thus their sensitivity constants, are un-measured and difficult to calculate. In this case Eq. (A4) can limit the possible range of  $n_{\text{tot}}$  instead of calculating it exactly. Rewriting Eq. (A4) gives

$$\int n_{\text{tot}} dl = \frac{\Delta\phi_{\text{tot}}}{C_e [\bar{Z} - \text{Err}]}, \quad (\text{A6})$$

where  $\text{Err} = 0$  gives the lower bound for  $n_{\text{tot}}$ ,

$$\left( \int n_{\text{tot}} dl \right)_{\min} = \frac{\Delta\phi_{\text{tot}}}{C_e \bar{Z}}, \quad (\text{A7})$$

and the upper bound of  $n_{\text{tot}}$  corresponds to the upper bound on the error defined as  $\text{Err}_{\max}$ ,

$$\left( \int n_{\text{tot}} dl \right)_{\max} = \frac{\Delta\phi_{\text{tot}}}{C_e [\bar{Z} - \text{Err}_{\max}]}. \quad (\text{A8})$$

The maximum correction is

$$\text{Err}_{\max} = \frac{C_{\max}}{C_e} \geq \sum_{j,k} \frac{C_{0,k}}{C_e} \frac{n_{j,k}}{n_{\text{tot}}} \geq \sum_{j,k} \frac{C_{j,k}}{C_e} \frac{n_{j,k}}{n_{\text{tot}}} = \text{Err},$$

where  $C_{\max}$  is the largest sensitivity constant for all the gas species and ionization states present. The sensitivity constant  $C_{j,k}$  for any gas species  $k$  is directly proportional to the Slater screening constant  $K$ , i.e.,  $C_{j,k} = (2\pi K_{j,k} m_k) / \lambda$ , where  $\lambda$  is the interferometer laser wavelength. The  $K$  is proportional to the sum of mean square electron orbits for all bound electrons<sup>52</sup>, and thus, for a given gas species  $k$ , the largest  $K$  occurs for the neutral atom. Thus,  $C_{\max} = C_{0,k}$  for the gas species  $k$  with the largest neutral sensitivity constant. The maximum correction factor is then<sup>37</sup>

$$\text{Err}_{\max} = \frac{(C_{0,k})_{\max}}{C_e} = \frac{2\pi}{C_e \lambda} (K_{0,k} m_k)_{\max} \quad (\text{A9})$$

$$= \frac{2\pi}{C_e \lambda} \left( \frac{\delta N_n^{STP}}{n_n^{STP}} \right)_{k,\max}, \quad (\text{A10})$$

where  $n_n^{STP}$  is the neutral density of the species at standard temperature and pressure,  $N_n$  is the refractive index of the neutral species,  $\delta N_n = N_n - 1$ , and  $C_e = \lambda e^2 / (4\pi \epsilon_0 m_e c^2)$ .

<sup>1</sup>E. C. Merritt, A. L. Moser, S. C. Hsu, J. Loverich, and M. A. Gilmore, Phys. Rev. Lett. **111**, 085003 (2013).

<sup>2</sup>S. C. Hsu, E. C. Merritt, A. L. Moser, T. J. Awe, S. J. E. Brockington, J. S. Davis, C. S. Adams, A. Case, J. T. Cassibry, J. P. Dunn, M. A. Gilmore, A. G. Lynn, S. J. Messer, and F. D. Witherspoon, Phys. Plasmas **19**, 123514 (2012).

<sup>3</sup>S. C. Hsu, T. J. Awe, S. Brockington, A. Case, J. T. Cassibry, G. Kagan, S. J. Messer, M. Stanic, X. Tang, D. R. Welch, and F. D. Witherspoon, IEEE Trans. Plasma Sci. **40**, 1287 (2012).

<sup>4</sup>J. T. Cassibry, M. Stanic, S. C. Hsu, F. D. Witherspoon, and S. I. Abarzhi, Phys. Plasmas **19**, 052702 (2012).

<sup>5</sup>J. T. Cassibry, M. Stanic, and S. C. Hsu, Phys. Plasmas **20**, 032706 (2013).

<sup>6</sup>Y. C. F. Thio, E. Panarella, R. C. Kirkpatrick, C. E. Knapp, F. Wysocki, P. Parks, and G. Schmidt, in *Current Trends in International Fusion Research—Proceedings of the Second International Symposium*, edited by E. Panarella (NRC Canada, Ottawa, 1999) p. 113.

<sup>7</sup>Y. C. F. Thio, C. E. Knapp, R. C. Kirkpatrick, R. E. Siemon, and P. J. Turchi, J. Fusion Energy **20**, 1 (2001).

<sup>8</sup>I. R. Lindemuth and R. C. Kirkpatrick, Nucl. Fusion **23**, 263 (1983).

<sup>9</sup>R. C. Kirkpatrick, I. R. Lindemuth, and M. S. Ward, Fusion Tech. **27**, 201 (1995).

<sup>10</sup>I. R. Lindemuth and R. E. Siemon, Amer. J. Phys. **77**, 407 (2009).

<sup>11</sup>R. P. Drake, *High-Energy-Density-Physics* (Springer, Berlin, 2006).

<sup>12</sup>T. J. Awe, C. S. Adams, J. S. Davis, D. S. Hanna, S. C. Hsu, and J. T. Cassibry, Phys. Plasmas **18**, 072705 (2011).

<sup>13</sup>A. Case, S. Messer, S. Brockington, L. Wu, F. D. Witherspoon, and R. Elton, Phys. Plasmas **20**, 012704 (2013).

<sup>14</sup>S. Messer, A. Case, L. Wu, S. Brockington, and F. D. Witherspoon, Phys. Plasmas **20**, 032306 (2013).

- <sup>15</sup>W. Linchun, M. Phillips, S. Messer, A. Case, and F. D. Witherspoon, *IEEE Trans. Plasma Sci.* **41**, 1011 (2013).
- <sup>16</sup>M. Y. Jaffrin and R. F. Probstein, *Phys. Fluids* **7**, 1658 (1964).
- <sup>17</sup>R. A. Bosch, R. L. Berger, B. H. Failor, N. D. Delamater, G. Charatis, and R. L. Kauffman, *Phys. Fluids B* **4**, 979 (1992).
- <sup>18</sup>O. Rancu, P. Renaudin, C. Chenais-Popovics, H. Kawagashi, J. C. Gauthier, M. Dirksmoller, T. Missalla, I. Uschmann, E. Forster, O. Larroche, O. Peyrusse, O. Renner, E. Krousky, H. Pepin, and T. Shepard, *Phys. Rev. Lett.* **75**, 3854 (1995).
- <sup>19</sup>A. S. Wan, T. W. Barbee, Jr., R. Cauble, P. Celliers, L. B. Da Silva, J. C. MOrno, P. W. Rambo, G. F. Stone, J. E. Trebes, and F. Weber, *Phys. Rev. E* **55**, 6293 (1997).
- <sup>20</sup>N. C. Woolsey, Y. Abou, R. G. Evans, R. A. D. Grundy, S. J. Pestehe, P. G. Carolan, N. J. Conway, R. O. Dendy, P. Helander, K. G. McClements, J. G. Kirk, P. A. Norreys, M. M. Notley, and S. J. Rose, *Phys. Plasmas* **8** (2001).
- <sup>21</sup>L. Romagnani, S. V. Bulanov, M. Borghesi, P. Audebert, J. C. Gauthier, K. Lowenbruck, A. J. Mackinnon, P. Patel, G. Pretzler, T. Toncian, and O. Willi, *Phys. Rev. Lett.* **101**, 025004 (2008).
- <sup>22</sup>Y. Kuramitsu, Y. Sakawa, T. Morita, C. D. Gregory, J. N. Waugh, S. Dono, H. Aoki, H. Tanji, M. Koenig, N. Woolsey, and H. Takabe, *Phys. Rev. Lett.* **106**, 175002 (2011).
- <sup>23</sup>N. Kugland, D. D. Ryutov, P.-Y. Chang, R. P. Drake, G. Fiksel, D. H. Froula, S. H. Glenzer, G. Gregori, M. Grosskopf, M. Koenig, Y. Kuramitsu, C. Kuranz, M. C. Levy, E. Liang, J. Meinecke, F. Miniati, T. Morita, A. Pelka, C. Plechaty, R. Presura, A. Ravasio, B. A. Remington, B. Reville, J. S. Ross, Y. Sakawa, A. Spitkovsky, H. Takabe, and H.-S. Park, *Nature Phys.* **8**, 809 (2012).
- <sup>24</sup>J. S. Ross, S. H. Glenzer, P. Amendt, R. Berger, L. Divol, N. L. Kugland, O. L. Landen, C. Plechaty, B. Remington, D. Ryutov, W. Rozmus, D. H. Froula, G. Fiksel, C. Sorce, Y. Kuramitsu, T. Morita, Y. Sakawa, H. Takabe, R. P. Drake, M. Grosskopf, C. Kuranz, G. Gregori, J. Meinecke, C. D. Murphy, M. Koenig, A. Pelka, A. Ravasio, T. Vinci, E. Liang, R. Presura, A. Spitkovsky, F. Miniati, and H.-S. Park, *Phys. Plasmas* **19**, 056501 (2012).
- <sup>25</sup>G. F. Swadling, S. V. Lebedev, N. Niasse, J. P. Chittenden, G. N. Hall, F. Suzuki-Vidal, G. Burkiak, A. J. Harvey-Thompson, S. N. Bland, P. De Grouch, E. Khoory, L. Pickworth, J. Skidmore, and L. Suttle, *Phys. Plasmas* **20**, 022705 (2013).
- <sup>26</sup>G. F. Swadling, S. V. Lebedev, G. N. Hall, F. Suzuki-Vidal, G. Burdiak, A. J. Harvey-Thompson, S. N. Bland, P. De Grouchy, E. Khoory, L. Pickworth, J. Skidmore, and L. Suttle, *Phys. Plasmas* **20**, 062706 (2013).
- <sup>27</sup>H. Luna, K. D. Kavanagh, and J. T. Costello, *J. Appl. Phys.* **101**, 033302 (2007).
- <sup>28</sup>C. Sánchez-Aké, D. Mustri-Trejo, T. García-Fernández, and M. Villagrán-Muniz, *Spectrochimica Acta B* **65**, 401 (2010).
- <sup>29</sup>P. Hough, C. McLoughlin, T. J. Kelly, P. Hayden, S. S. Harilal, J. P. Mosnier, and J. T. Costello, *J. Phys. D: Appl. Phys.* **42**, 055211 (2009).
- <sup>30</sup>P. Hough, C. McLoughlin, S. S. Harilal, J. P. Mosnier, and J. T. Costello, *J. Appl. Phys.* **107**, 024904 (2010).
- <sup>31</sup>P. Yeates, C. Fallon, E. T. Kennedy, and J. T. Costello, *Phys. Plasmas* **18** (2011).
- <sup>32</sup>R. L. Berger, J. R. Albritton, C. J. Randall, E. A. Williams, W. L. Kruer, A. B. Langdon, and C. J. Hanna, *Phys. Fluids B* **3**, 3 (1991).
- <sup>33</sup>S. M. Pollaine, R. L. Berger, and C. J. Keane, *Phys. Fluids B* **4**, 989 (1992).
- <sup>34</sup>P. W. Rambo and J. Denavit, *Phys. Plasmas* **1**, 4050 (1994).
- <sup>35</sup>P. W. Rambo and R. J. Proccassini, *Phys. Plasmas* **2**, 3130 (1995).
- <sup>36</sup>E. C. Merritt, A. G. Lynn, M. A. Gilmore, and S. C. Hsu, *Rev. Sci. Instrum.* **83**, 033506 (2012).
- <sup>37</sup>E. C. Merritt, A. G. Lynn, M. A. Gilmore, C. Thoma, J. Loverich, and S. C. Hsu, *Rev. Sci. Instrum.* **83**, 10D523 (2012).
- <sup>38</sup>L. D. Landau and E. M. Lifshitz, *Fluid Mechanics 2nd Ed.* (Butterworth-Heinemann, 2011) pp. 313–350.
- <sup>39</sup>R. H. Nunn, *Intermediate Fluid Dynamics* (Hemisphere Publishing, New York, 1989) pp. 128–134.
- <sup>40</sup>M. J. Weber, *Handbook of Optical Materials*, 1st ed. (CRC Press, Boca Raton, 2003) pp. 447–449.
- <sup>41</sup>D. R. Lide, *Handbook of Chemistry and Physics*, 83rd ed. (CRC Press, Boca Raton, 2002–2003) pp. 4–39–4–96.
- <sup>42</sup>A. V. Ivanova and V. N. Kologrivov, *J. Appl. Spect.* **13**, 961 (1970).
- <sup>43</sup>A. D. Rakić, *Appl. Optics* **34**, 4755 (1995).
- <sup>44</sup>J. J. MacFarlane, I. E. Golovkin, P. R. Woodruff, D. R. Welch, B. V. Oliver, T. A. Mehlhorn, and R. B. Campbell, in *Inertial Fusion Sciences and Applications 2003*, edited by B. A. Hammel, D. D. Meyerhofer, and J. Meyer-ter-Vehn (American Nuclear Society, La Grange Park, IL, 2004) p. 457.
- <sup>45</sup>J. D. Huba, *NRL Plasma Formulary*, 2011.
- <sup>46</sup>A. V. Phelps, *J. Phys. Chem. Ref. Data* **20**, 557 (1990).
- <sup>47</sup>J. T. Cassibry, R. J. Cortez, S. C. Hsu, and F. D. Witherspoon, *Phys. Plasmas* **16**, 112707 (2009).
- <sup>48</sup>J. F. Santarius, *Phys. Plasmas* **19**, 072705 (2012).
- <sup>49</sup>P. B. Parks, *Phys. Plasmas* **15**, 062506 (2008).
- <sup>50</sup>H. Kim, L. Zhang, R. Samulyak, and P. Parks, *Phys. Plasmas* **20**, 022704 (2013).
- <sup>51</sup>J. S. Davis, S. C. Hsu, I. E. Golovkin, J. J. MacFarlane, and J. T. Cassibry, *Phys. Plasmas* **19**, 102701 (2012).
- <sup>52</sup>R. A. Alpher and D. R. White, *Phys. Fluids* **2**, 153 (1959).